Lattice distortion associated with Fermi-surface reconstruction in $Sr_3Rh_4Sn_{13}$

C. N. Kuo,[1] C. W. Tseng,[1] C. M. Wang,[1] C. Y. Wang,[2] Y. R. Chen,[2] L. M. Wang,[2,*]
C. F. Lin,[3] K. K. Wu,[3] Y. K. Kuo,[3,†] and C. S. Lue[1,4,‡]

[1]*Department of Physics, National Cheng Kung University, Tainan 70101, Taiwan*
[2]*Department of Physics, National Taiwan University, Taipei 10601, Taiwan*
[3]*Department of Physics, National Dong Hwa University, Hualien 97401, Taiwan*
[4]*Taiwan Consortium of Emergent Crystalline Materials, Ministry of Science and Technology, Taipei 10601, Taiwan*

(Received 5 January 2015; revised manuscript received 16 March 2015; published 30 April 2015)

Superconducting $Sr_3Rh_4Sn_{13}$ has been of current interest due to indications of a characteristic phase transition associated with structural distortions in its normal state. To further shed light on the nature of the phase transition, we performed a detailed study of single crystalline $Sr_3Rh_4Sn_{13}$ by means of the thermal expansion, electrical resistivity, Hall coefficient, Seebeck coefficient, thermal conductivity, as well as ^{119}Sn nuclear magnetic resonance (NMR) measurements, mainly focusing on the signatures around the phase transition temperature $T^* = 137$ K. The phase transition has been characterized by marked features near T^* in all measured physical quantities. In particular, the NMR characteristics provide microscopic evidence for the reduction in the electronic Fermi-level density of states (DOSs) below T^*. Based on the analysis of the ^{119}Sn NMR spin-lattice relaxation rate, we clearly demonstrated that the Sn 5*s* partial Fermi-level DOS in $Sr_3Rh_4Sn_{13}$ is reduced by 13% across the phase transition. In this respect, it points to the strong association between electronic and structural instability for the peculiar phase transition in $Sr_3Rh_4Sn_{13}$.

DOI: 10.1103/PhysRevB.91.165141 PACS number(s): 71.27.+a, 71.20.Lp, 76.60.−k

I. INTRODUCTION

Superconducting stannides with a $Yb_3Rh_4Sn_{13}$-type structure (space group $Pm\bar{3}n$) continue to attract attention in the field of solid state physics due to indications of unconventional superconductivity and peculiar behavior in the normal states [1–16]. Among these superconductors, $Ca_3Ir_4Sn_{13}$, $Sr_3Ir_4Sn_{13}$, and $La_3Co_4Sn_{13}$ are prominent members showing exotic phase transitions in their normal states [1,3–7,10–14]. Marked features have been observed near $T^* \simeq 35$ K, 147 K, and 152 K in $Ca_3Ir_4Sn_{13}$, $Sr_3Ir_4Sn_{13}$, and $La_3Co_4Sn_{13}$, respectively [1,3,5,7,10–14]. Single crystal x-ray diffraction (XRD) analysis for $Sr_3Ir_4Sn_{13}$below and above T^* reveals the presence of a structural change, driven by the lattice distortion with a lattice parameter twice than that of the high-temperature phase [5]. With respect to the facts that no magnetic origin involved in the structural transition and a substantial Fermi-surface reduction below T^*, the observed lattice distortion in $Sr_3Ir_4Sn_{13}$ has been associated with the charge-density-wave (CDW) instability [5,10,12,13]. The scenario for the lattice distortion accompanied with the CDW formation below T^* has also been proposed for the isostructural compounds of $Ca_3Ir_4Sn_{13}$ and $La_3Co_4Sn_{13}$ [6–8,11,16].

The titled compound of $Sr_3Rh_4Sn_{13}$, which also adopts the $Pm\bar{3}n$ structure at room temperature, has been found to be a superconductor with a superconducting transition temperature T_c of about 4.2 K [2,17]. According to the low-temperature specific heat measurement, $Sr_3Rh_4Sn_{13}$ was categorized as a strongly coupling nodeless superconductor [2]. A very recent reexamination of this compound indicates an evident phase transition at $T^* \simeq 138$ K, along with a spiky peak in the specific heat and a distinct hump in the electrical resistivity near T^* [18]. Based on the weak superlattice reflections in the single crystal XRD data below T^*, the observed phase transition has been interpreted as a structural transition from cubic $Pm\bar{3}n$ to $I\bar{4}3d$, involving crystallographic cell doubling [18]. Theoretical density functional theory (DFT) calculations of the phonon dispersion in $Sr_3Rh_4Sn_{13}$ indicated that the primary lattice instabilities arise from phonon modes with wave vectors $\mathbf{q} = (0.5,0,0)$ at the X point and $\mathbf{q} = (0.5,0.5,0)$ at the M point of the corresponding Brillioun zone [18]. In addition, a systematic suppression in T^* accompanied with an enhancement in T_c has been established by introducing the hydrostatic pressure and chemical pressure in this material, revealing the important interplay between the structural distortion and superconductivity in $Sr_3Rh_4Sn_{13}$ [18].

To elucidate the nature of the structural distortion in $Sr_3Rh_4Sn_{13}$, we carried out various experiments including the thermal expansion, electrical resistivity (ρ), Hall coefficient (R_H), Seebeck coefficient (S), thermal conductivity (κ), as well as nuclear magnetic resonance (NMR) measurements, focusing on the temperature region in the vicinity of T^*. Pronounced features near $T^* = 137$ K have been discerned in the temperature dependencies of the bulk properties. The obtained Hall carrier concentration n_H exhibits a prominent change in both sign and magnitude at around T^*, indicating a significant reconstruction of the electronic bands across the phase transition. The Seebeck coefficient, a sensitive probe of the Fermi surfaces, also implies a modification of the electronic band structure below T^*. The analysis of the thermal conductivity suggests that the abrupt change in κ near T^* is essentially caused by the reduction of the electronic contribution. The NMR characteristics further provide microscopic evidence for the decrease in both Rh 4*d* and Sn 5*s* electronic Fermi-level density of states (DOSs) below T^*. With the analysis of the ^{119}Sn NMR spin-lattice relaxation rate, we clearly demonstrated that the Sn 5*s* partial

*liminwang@ntu.edu.tw
†ykkuo@mail.ndhu.edu.tw
‡cslue@mail.ncku.edu.tw

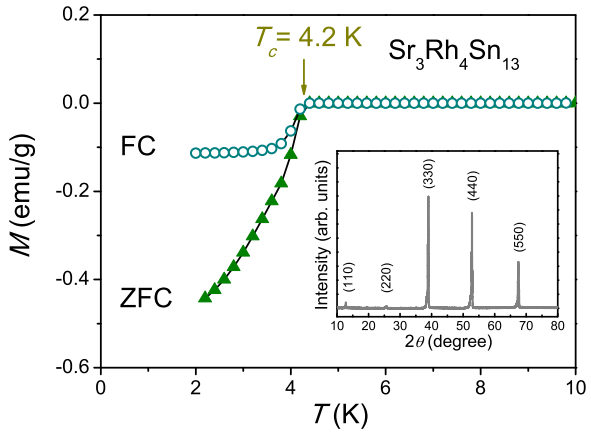

FIG. 1. (Color online) Temperature dependence of M under zero-field-cooled (ZFC) and field-cooled (FC) processes for $Sr_3Rh_4Sn_{13}$. The arrow indicates the superconducting transition temperature $T_c = 4.2$ K. The inset gives a room-temperature single crystal x-ray diffraction pattern from the (110) plane of $Sr_3Rh_4Sn_{13}$. Reflections are indexed with respect to the $Yb_3Rh_4Sn_{13}$-type structure (space group $Pm\bar{3}n$).

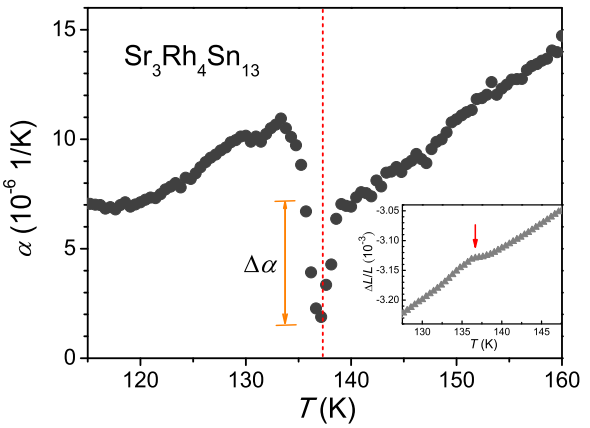

FIG. 2. (Color online) Coefficient of linear thermal expansion α for $Sr_3Rh_4Sn_{13}$ as a function of temperature. The dashed line indicates the phase transition temperature $T^* = 137$ K. (Inset) Plot of $\Delta L/L$ vs T in the vicinity of T^*, as indicated by the arrow.

Fermi-level DOS in $Sr_3Rh_4Sn_{13}$ is reduced by approximately 13% across the phase transition.

II. EXPERIMENTAL RESULTS AND DISCUSSION

Single crystals of $Sr_3Rh_4Sn_{13}$ were grown by the Sn self-flux method. High purity elements were mixed in the molar ratio of Sr:Rh:Sn = 1:1.5:11 and sealed in an evacuated quartz tube. The tube was heated up to 1050 °C, and then cooled to 600 °C over 72 h. The excessive Sn flux was etched in diluted hydrochloric acid. The resulting crystals have dimensions of several millimeters. A room-temperature XRD measurement taken with Cu K_α radiation on a single crystalline specimen was identified within the expected $Pm\bar{3}n$ phase, with a lattice constant $a = 9.7909$ Å. For the transport measurements, the electrical current flows along the direction perpendicular to the (110) plane of the crystal which has been identified by the XRD with the result given in the inset of Fig. 1.

A. Bulk properties

Magnetization (dc) M measurements were carried out using a SQUID magnetometer measured with a small field of 10 Oe under zero-field-cooled (ZFC) and field-cooled (FC) processes. The observed diamagnetic behavior below $T_c = 4.2$ K confirms the occurrence of superconductivity in $Sr_3Rh_4Sn_{13}$. Here T_c was taken as the onset of the diamagnetic response in the magnetization data, as indicated by the arrow in Fig. 1.

The linear thermal expansivity was measured using a capacitance dilatometer which was calibrated against standard copper and aluminum samples. The relative sensitivity of our dilatometer is about 10^{-10} for the sample of similar dimensions. The determined coefficient of linear thermal expansion α for $Sr_3Rh_4Sn_{13}$ is illustrated in Fig. 2, and the inset shows a close-up plot of the thermal expansivity $\Delta L/L$ in the vicinity of the transition. It is remarkable that a pronounced dip in α appears at the onset of the phase transition. We thus determined the transition temperature $T^* = 137$ K using the position of the negative dip for $Sr_3Rh_4Sn_{13}$.

According to the Ehrenfest relation [19], the variation of the thermal expansion $\Delta\alpha$ can be related to the specific heat change ΔC_p and the pressure-dependent transition temperature dT^*/dP as

$$\Delta\alpha = \frac{1}{3V}\left(\frac{\Delta C_p}{T^*}\right)\left(\frac{dT^*}{dP}\right). \quad (1)$$

Substituting the values of $\Delta\alpha \simeq -5.6 \times 10^{-6}$ K^{-1}, $\Delta C_p \simeq 30$ J/mol − K (estimated from Ref. [18]), $T^* = 137$ K, and the molar volume $V = 2.83 \times 10^{-4}$ m^3/mol to Eq. (1), it yields $dT^*/dP = -2.3$ K/kbar which agrees very well with the experimental result ($\simeq -2.2$ K/kbar) taken by Goh *et al.* [18]. The rather high suppression of T^* under hydrostatic pressure for $Sr_3Rh_4Sn_{13}$ suggests that the structural distortion is associated with very soft phonon modes. Such a scenario has been proposed by Tompsett *et al.* based on their calculations for the phonon dispersion relation of $Sr_3Rh_4Sn_{13}$ [18]. Accordingly, the lattice instability accompanied by the soft phonon modes would play a major role for stabilizing the superconductivity of this material.

Electrical resistivity obtained using a standard four-point probe method, as a function of temperature for $Sr_3Rh_4Sn_{13}$ is displayed in Fig. 3. The temperature dependence of ρ features a distinct hump below $T^* = 137$ K and a superconducting phase transition at $T_c = 4.2$ K, being consistent with those reported in the literature [2,17,18]. The normal state resistivity between 6 and 30 K can be described well to a power law,

$$\rho(T) = \rho_o + AT^2, \quad (2)$$

where ρ_o is the residual resistivity and A is the temperature coefficient of the electric resistivity. In the inset of Fig. 3, we showed the plot of ρ vs T^2, with the linear relation yielding $\rho_o = 8.6$ $\mu\Omega$ − cm and $A = 0.014$ $\mu\Omega$ − cm/K^2. The residual resistivity ρ_o may arise from the scattering due to domain boundaries and/or defects by electrons. The small value of ρ_o indicates the high quality of the present single

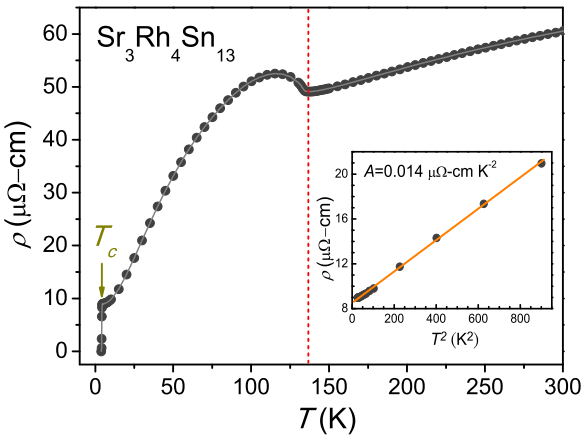

FIG. 3. (Color online) Electrical resistivity ρ as a function of temperature for $Sr_3Rh_4Sn_{13}$. The dashed vertical line highlights the position of T^*. The inset displays a plot of ρ vs T^2, showing a linear relation between 6 and 30 K.

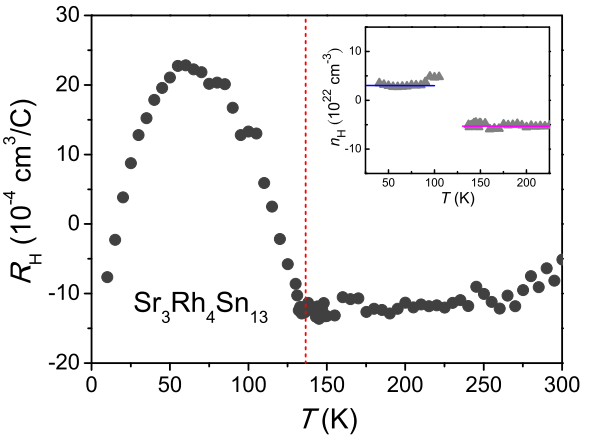

FIG. 4. (Color online) Hall resistivity as a function of temperature for $Sr_3Rh_4Sn_{13}$ measured at $H = 3$ T. The inset shows the temperature dependence of the Hall carrier concentration n_H. Each horizontal straight line indicates the value of n_H.

crystal, and gives an estimate of the residual resistivity ratio [RRR, $\rho(300\ \mathrm{K})/\rho_o$] of about 7.1 for our single crystalline $Sr_3Rh_4Sn_{13}$. In principle, the magnitude of A can be employed to judge the strength of the electronic correlation of the studied system [20]. Taking $A = 0.014\ \mu\Omega - \mathrm{cm/K^2}$ and the low-temperature specific heat coefficient $\gamma = 31\ \mathrm{mJ/mol - K^2}$ extracted by Kase *et al.* [2], we obtained the Kadowaki-Woods ratio $A/\gamma^2 = 1.46 \times 10^{-5}\ \mu\Omega - \mathrm{cm/(mJ/mol - K^2)^2}$ for $Sr_3Rh_4Sn_{13}$. This value is close to those observed in a variety of known strongly correlated systems [21], which generally have a Kadowaki-Woods relation $A/\gamma^2 \simeq 1 \times 10^{-5}\ \mu\Omega - \mathrm{cm/(mJ/mol - K^2)^2}$.

For the Hall coefficient measurement, five leads were soldered with indium and a Hall-measurement geometry was constructed to allow simultaneous measurements of both longitudinal (ρ_{xx}) and transverse (Hall) resistivities (ρ_{xy}) using standard dc techniques. The contact size was miniaturized as small as possible (<0.2 mm) to avoid large inaccuracy in the determination of resistivities. Hall voltages were taken in opposing fields up to 6 T and with an in-plane current density of about 60 $\mathrm{A/cm^2}$.

Temperature dependence of the Hall coefficient R_H for $Sr_3Rh_4Sn_{13}$ measured at a constant field $H = 3$ T is shown in Fig. 4. The negative sign in R_H at high temperatures indicates that the electron-type carriers dominate its electrical transport. Upon further cooling, a sharp change in R_H takes place below T^*. The strong temperature variation of R_H suggests a multiband character of the Fermi surfaces. Here, a simple two-band picture is sufficient for the realization of the Fermi-surface structure as

$$R_H = \frac{\sigma_n^2 R_n + \sigma_p^2 R_p}{(\sigma_n + \sigma_p)^2}, \tag{3}$$

where $R_{n,p}$ and $\sigma_{n,p}$ represent the Hall coefficients and electrical conductivities for the n- and p-type carriers from electronic and hole bands, respectively. In principle, each parameter is governed by the scattering relaxation time which varies differently with temperature. At low temperatures, the p-type carriers have a dominant contribution, leading to a positive sign in R_H. A noticeable downturn in R_H appears at around 60 K, implying that multiscattering channels are involved. Similar peak features have been reported in the d-electron heavy fermion compound LiV_2O_4, the two-gap superconductor $Lu_2Fe_3Si_5$, and the strong coupling superconductor $SrPt_3P$ [22–24], suggesting the importance of the strongly correlated effect on the low-temperature state of $Sr_3Rh_4Sn_{13}$.

The inset of Fig. 4 illustrates the temperature dependence of the Hall carrier concentration n_H, estimated from $1/R_He$, away from the transition region. We obtained the values of $n_H \simeq -5.3 \times 10^{22}\ \mathrm{cm^{-3}}$ above T^* and $n_H \simeq 3.1 \times 10^{22}\ \mathrm{cm^{-3}}$ below T^* for $Sr_3Rh_4Sn_{13}$. The prominent changes in both sign and magnitude of n_H indicate a significant modification of the electronic band structure across the phase transition. Accordingly, the decrease in the magnitude of n_H could be realized as Fermi-surface reduction associated with the superlattice distortion. The abrupt decrease in the carrier density below T^* has also been found in $Sr_3Ir_4Sn_{13}$, indicating a similar mechanism responsible for the phase transition in both systems [10].

Seebeck coefficient and thermal conductivity experiments were simultaneously performed in a closed cycle refrigerator using a heat pulse technique. Further details about the experimental techniques for these measurements can be found elsewhere [25]. It is known that the Seebeck coefficient is a sensitive probe for the phenomenon associated with changes in the Fermi surfaces such as the CDW ordering and crystallographic distortion [25–28]. The plot of the measured Seebeck coefficient as a function of temperature for $Sr_3Rh_4Sn_{13}$ is given in Fig. 5. As one can see, the strong temperature variation of S reveals evidence for the presence of a multiband effect. We thus employed a two-band model as in the case for the Hall coefficient analysis as

$$S = \frac{\sigma_n S_n + \sigma_p S_p}{\sigma_n + \sigma_p},$$

where $S_{n,p}$ are the Seebeck coefficients for the n- and p-type carriers, respectively. For $T < T^*$, the positive sign of S signifies that the hole-type carriers dominate the thermoelectric transport, being consistent with the observation from the Hall

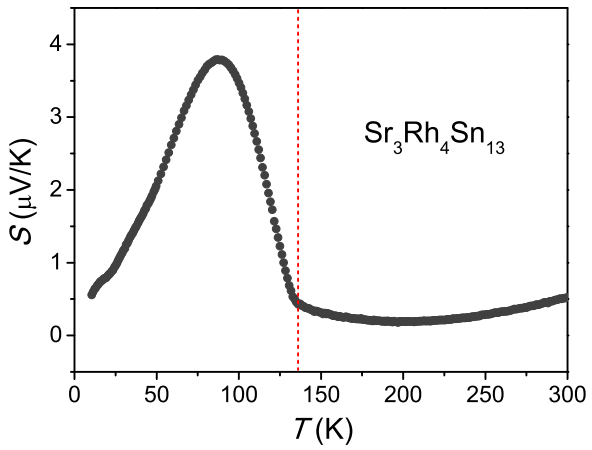

FIG. 5. (Color online) Temperature dependence of the Seebeck coefficient S for $Sr_3Rh_4Sn_{13}$. The dashed vertical line indicates the position of T^*.

measurement. In the vicinity of T^*, a drastic change in the feature of S has been noticed. This phenomenon can be understood by an increasing contribution from the n-type carriers, indicating substantial modification in the Fermi surfaces across the phase transition. It is found that the measured Seebeck coefficient is small but remains positive (<0.5 μV/K) while Hall coefficient changes sign to negative above T^*. Such a finding suggests that the electrical conductivity for the n-type carrier becomes dominating over the p-type carrier as $T > T^*$. It is noticeable that the $S(T)$ exhibits a broad peak at around 80 K in $Sr_3Rh_4Sn_{13}$. Similar features have also been noted in $Sr_3Ir_4Sn_{13}$ near 110 K and in the CDW systems of $Bi_2Rh_3Se_2$ and $SmNiC_2$ near 95 K and 110 K, respectively [10,29,30]. Since the magnitude of S is inversely proportional to the electronic DOS at round the Fermi level, the enhancement in S can be attributed to the decrease in the Fermi-level DOS below T^*, presumably associated with CDW ordering.

Figure 6 illustrates the temperature dependence of the thermal conductivity κ for $Sr_3Rh_4Sn_{13}$. With decreasing

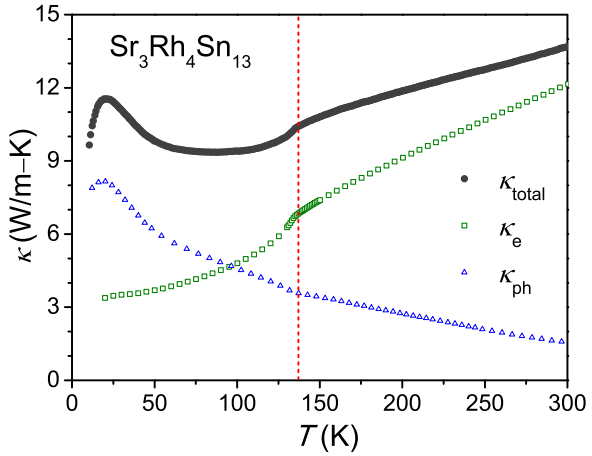

FIG. 6. (Color online) Temperature variation of the total thermal conductivity κ for $Sr_3Rh_4Sn_{13}$. The electronic thermal conductivity κ_e was evaluated using the Wiedemann-Franz raw. The lattice thermal conductivity κ_L was obtained by subtracting κ_e from the experimental κ.

temperature, a marked drop in κ was observed near T^*. In principle, the total thermal conductivity for an ordinary metal is a sum of electronic and lattice terms. The electronic thermal conductivity (κ_e) can be evaluated using the Wiedemann-Franz law $\kappa_e\rho/T = L_o$, where ρ is the experimental dc electric resistivity and $L_o = 2.45 \times 10^{-8}$ WΩ K^{-2} is the theoretical Lorenz number. The extracted T-dependent κ_e for $Sr_3Rh_4Sn_{13}$ is displayed in Fig. 6. Remarkably, κ_e also exhibits a kink at around T^*, and the feature is nearly identical to the observed κ. This analysis thus provides a confirmation that the abrupt change in κ near T^* is essentially caused by the reduction of the electronic contribution for $Sr_3Rh_4Sn_{13}$.

The lattice thermal conductivity (κ_L), obtained by subtracting κ_e from the experimental κ, is also given in Fig. 6. It is worthwhile mentioning that a relatively low room-temperature $\kappa_L \simeq 1.58$ W/m $-$ K was found. Such a result can be realized as the enhanced phonon scattering due to the cagelike crystallographic structure for $Sr_3Rh_4Sn_{13}$. The reduction in κ_L is plausibly suppressed by the rattling of the loose atoms within the crystallographic cages.

B. Nuclear magnetic resonance

Nuclear magnetic resonance is known as a site-selective tool, yielding the local information of structural and electronic characteristics for the studied materials [31–33]. In this investigation, NMR measurements were carried out using a Varian 300 spectrometer, with a constant field of 7.0868 T. To avoid the skin depth problem of the rf transmission power, we used a powder sample by crushing the single crystals of $Sr_3Rh_4Sn_{13}$. The specimen was put in a plastic vial that showed no observable ^{119}Sn NMR signal.

^{119}Sn (nuclear spin $I = 1/2$) NMR spectra which were mapped out by integrating the spin echo signal of various excitations, are displayed in Fig. 7. Within the $Yb_3Rh_4Sn_{13}$-type structure, there are two nonequivalent crystallographic Sn sites, denoted as Sn1 and Sn2. While the Sn1 atoms occupy the axially symmetric 2a site (in Wyckoff notations), the Sn2 atoms reside at the 24k site which is nonaxially symmetric. According to their site occupation, one expects to observe two ^{119}Sn NMR resonance lines with a lineshape area ratio of 1:12 for Sn1 and Sn2, respectively. We, however, only detected the dominant Sn2 resonance line, implying the similar atomic environments for both sites in $Sr_3Rh_4Sn_{13}$. Such an observation has also been reported in the isostructural compound $Ca_3Ir_4Sn_{13}$ [15].

To gain more insight into the evolution of the resonance line across the phase transition, we illustrate several representative spectra taken below and above T^*. The observed lineshapes below and above T^* can be reproduced from simulations, shown as dotted curves beneath the data points for 62 K and above the data for 247 K, respectively. It is apparent that the line width does not exhibit a dramatic broadening below T^*, signifying the absence of magnetic ordering across this phase transition.

Figure 8 shows the temperature dependence of the ^{119}Sn NMR Knight shift ^{119}K of $Sr_3Rh_4Sn_{13}$, determined from the simulated result of the individual NMR spectrum. The values of ^{119}K were referred to the ^{119}Sn resonance frequency $\nu_R = 112.519$ MHz, evaluated from the nuclear gyromagnetic

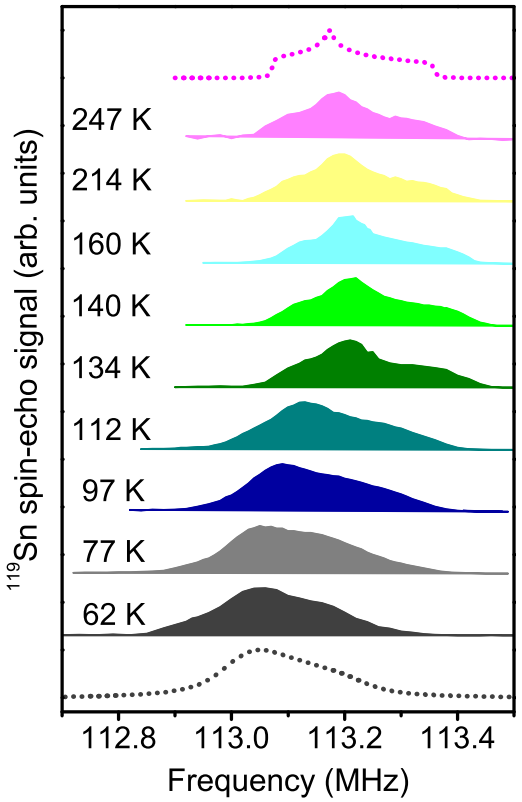

FIG. 7. (Color online) Evolution of ^{119}Sn NMR spectrum for $Sr_3Rh_4Sn_{13}$ measured at various temperatures. The dotted curves are simulated results corresponding to 247 K and 62 K, respectively.

ratio $^{119}\gamma_N/2\pi = 1.5867$ MHz/kOe. As one can see, the Knight shift changes progressively with a rapid decrease below T^*, consistent with the feature found in the bulk magnetic susceptibility χ given in the inset of Fig. 8. The Knight shift here is a sum of three parts as $^{119}K = K_{\rm orb} + K_s + K_{sd}$. The first term $K_{\rm orb}$ is the orbital shift due to the contribution from the Van Vleck orbital magnetism and the second one K_s arises from Sn s-character electrons. The effect arising from p electrons can be neglected, owing to the relatively weak

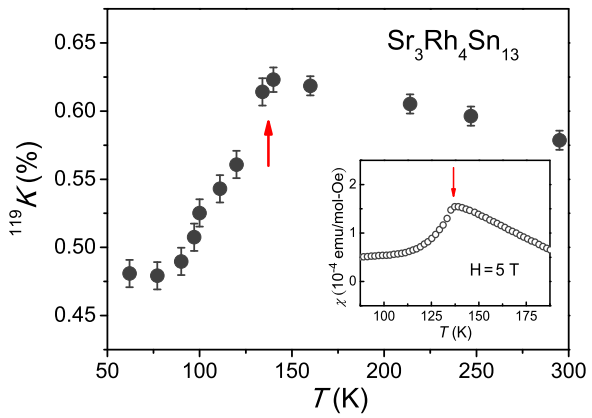

FIG. 8. (Color online) Temperature-dependent ^{119}Sn NMR Knight shift for $Sr_3Rh_4Sn_{13}$. The arrow indicates the phase transition temperature $T^* = 137$ K. The inset shows the magnetic susceptibility χ of $Sr_3Rh_4Sn_{13}$ in the vicinity of T^*.

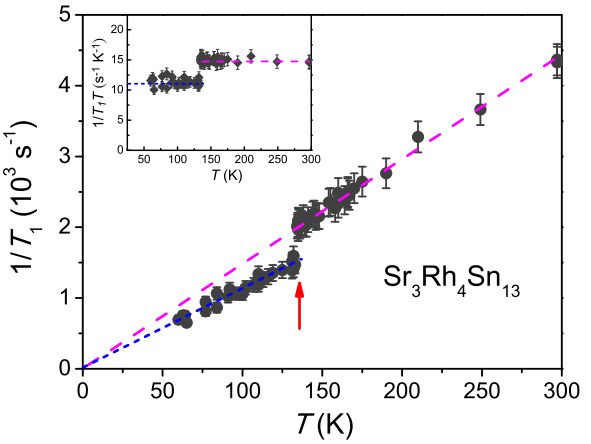

FIG. 9. (Color online) Temperature variation of the ^{119}Sn spin-lattice relaxation rate for $Sr_3Rh_4Sn_{13}$. Two straight lines indicate the linear behavior and the difference in the slope of $1/T_1$. (Inset) Plot of $1/T_1T$ vs T with two horizontal lines demonstrating the reduction in the magnitude of $1/T_1T$ across the phase transition.

core polarization from p orbitals [34,35]. The third term K_{sd} reflects the Rh $4d$electronic behavior through the transferred hyperfine interaction via conduction electrons. Therefore, the drop of the NMR Knight shift offers microscopic evidence that the reduction in χ is partially related to the decrease in the Sn $5s$ and Rh $4d$ electronic states of $Sr_3Rh_4Sn_{13}$.

While associating the Knight shift with specific electronic states is complicated by a mixture of hyperfine interactions and orbital shifts, the spin-lattice relaxation time (T_1) is comparatively simple as it is dominated by the conduction electrons, providing a direct and quantitative probe of Fermi-surface features for the paramagnetic cases [35–37]. The T_1 measurements were carried out using the saturation recovery method. We found each T_1 by centering the transmission frequency at the resonance line and recorded the signal strength by integrating the recovered spin echo signal. Each experimental T_1 was obtained by fitting to a single exponential recovery curve.

The main panel of Fig. 9 illustrates the temperature variation of the spin-lattice relaxation rate $1/T_1$ for $Sr_3Rh_4Sn_{13}$ with a marked change at around T^*. It is found that $1/T_1$ obeys the Korringa relation (constant T_1T) below and above T^*, being consistent with the paramagnetic nature of $Sr_3Rh_4Sn_{13}$. We thus provided the plot of $1/T_1T$ as a function of temperature in the inset of Fig. 9, which shows a clear reduction in $1/T_1T$ at T^* . From the magnitude of $1/T_1T$, we could estimate the Sn $5s$ partial Fermi level DOS as

$$\left(\frac{1}{T_1T}\right) = 2hk_B\left[\gamma_n H^s_{\rm hf} N_s(E_F)\right]^2, \qquad (4)$$

where h and k_B are the Planck constant and the Boltzmann constant, respectively. γ_n is the Sn nuclear gyromagnetic ratio, N_s (E_F) is the partial Sn $5s$ DOS at E_F in units of states/eV −spin, and $H^s_{\rm hf}$ represents the hyperfine field per spin of the Sn s electrons. Taking $H^s_{\rm hf} \sim 1.28 \times 10^7$ Gauss in Sn metals [34], each $N_s(E_F)$ can be extracted from the corresponding value of $1/T_1T$. We thus deduced $N_s(E_F) = 0.857$ states/eV − f.u. for $T > T^*$ and $N_s(E_F) = 0.745$ states/eV − f.u. for

$T < T^*$, corresponding to a 13% reduction in $N_s(E_F)$ across the phase transition. It is realistic that the Fermi-level electronic states of Sr $5s$, Sn $5p$, and Rh $4d$ in $Sr_3Rh_4Sn_{13}$ are also lowered by a similar factor.

The decrease in the electronic DOSs revealed from NMR further implies that a segment of the Fermi surfaces of $Sr_3Rh_4Sn_{13}$ is gapped below T^*. Because of the nonmagnetic nature of the phase transition at T^*, the present Fermi-level DOS reduction is reminiscent of the CDW formation arising from a Fermi-surface nesting [38–42]. Such a CDW scenario has been proposed for $Sr_3Ir_4Sn_{13}$ on the basis of the band structure calculation [5,9]. Accordingly, the calculated band No. 329 in $Sr_3Ir_4Sn_{13}$ exhibits a flat curvature region which is a strong candidate for the nesting of the Fermi surface. The contribution of this band to the real part of the wave vector dependent charge susceptibility $\chi(\mathbf{q})$ shows a peak at $\mathbf{q} = (1/2,1/2,1/2)$, implying a nesting instability with the wave vector $\mathbf{q} = (1/2,1/2,1/2)$ in $Sr_3Ir_4Sn_{13}$ [5,9]. Due to the crystallographic similarity, we speculate a possible modulation wave vector along the same direction of (1/2, 1/2, 1/2) in $Sr_3Rh_4Sn_{13}$. However, the unambiguous CDW state in $Sr_3Rh_4Sn_{13}$ will have to wait until the identification of charge modulation along a specific wave vector direction by means of a high resolution transmission electron microscopy (HRTEM) [43–46].

III. CONCLUDING REMARKS

Prominent features near $T^* = 137$ K of $Sr_3Rh_4Sn_{13}$ have been revealed in all measured physical quantities. Based on the pronounced signatures in α, ρ, R_H, S, and κ_e at around T^*, we obtained a precise picture that the characteristics of the phase transition are essentially related to the electronic state reconstruction at the Fermi surfaces. Furthermore, the NMR analyses provide a quantitative estimate that the Fermi-surface DOS is reduced by approximately 13% across the phase transition. The lack of significant NMR line broadening below T^* reinforces the conclusion that the phase transition is of no relevance to the magnetic ordering. Remarkably, the observed phase transition behavior in $Sr_3Rh_4Sn_{13}$ bears a striking resemblance to a CDW ordering in many aspects.

ACKNOWLEDGMENTS

This work was supported by the Ministry of Science and Technology of Taiwan under Grants No. MOST-103-2112-M-006-014-MY3 (C.S.L.), No. MOST-101-2112-M-002-020-MY2 (L.M.W.), No. MOST-103-2112-M-259-008-MY3 (YKK), and No. MOST-103-2119-M-006-014-MY3 (C.S.L.).

[1] J. Yang, B. Chen, C. Michioka, and K. Yoshimura, J. Phys. Soc. Jpn. **79**, 113705 (2010).
[2] N. Kase, H. Hayamizu, and J. Akimitsu, Phys. Rev. B **83**, 184509 (2011).
[3] K. Wang and C. Petrovic, Phys. Rev. B **86**, 024522 (2012).
[4] S. Y. Zhou, H. Zhang, X. C. Hong, B. Y. Pan, X. Qiu, W. N. Dong, X. L. Li, and S. Y. Li, Phys. Rev. B **86**, 064504 (2012).
[5] L. E. Klintberg, S. K. Goh, P. L. Alireza, P. J. Saines, D. A. Tompsett, P. W. Logg, J. Yang, B. Chen, K. Yoshimura, and F. M. Grosche, Phys. Rev. Lett. **109**, 237008 (2012).
[6] S. Gerber, J. L. Gavilano, M. Medarde, V. Pomjakushin, C. Baines, E. Pomjakushina, K. Conder, and M. Kenzelmann, Phys. Rev. B **88**, 104505 (2013).
[7] H. F. Liu, C. N. Kuo, C. S. Lue, K.-Z. Syu, and Y. K. Kuo, Phys. Rev. B **88**, 115113 (2013).
[8] A. Slebarski and J. Goraus, Phys. Rev. B **88**, 155122 (2013).
[9] D. A. Tompsett, Phys. Rev. B **89**, 075117 (2014).
[10] C. N. Kuo, H. F. Liu, C. S. Lue, L. M. Wang, C. C. Chen, and Y. K. Kuo, Phys. Rev. B **89**, 094520 (2014).
[11] A. Slebarski, M. Fijalkowski, M. M. Maska, M. Mierzejewski, B. D. White, and M. B. Maple, Phys. Rev. B **89**, 125111 (2014).
[12] A. F. Fang, X. B. Wang, P. Zheng, and N. L. Wang, Phys. Rev. B **90**, 035115 (2014).
[13] P. K. Biswas, A. Amato, R. Khasanov, H. Luetkens, Kefeng Wang, C. Petrovic, R. M. Cook, M. R. Lees, and E. Morenzoni, Phys. Rev. B **90**, 144505 (2014).
[14] L. M. Wang, C.-Y. Wang, G.-M. Chen, C. N. Kuo, and C. S. Lue, New J. Phys. **17**, 033005 (2015).
[15] R. Sarkar, F. Bruckner, M. Gunther, C. Petrovic, Kefeng Wang, P. K. Biswas, H. Luetkens, E. Morenzoni, A. Amato, and H.-H. Klauss, arXiv:1406.3544.
[16] S. K. Goh, L. E. Klintberg, P. L. Alireza, D. A. Tompsett, J. Yang, B. Chen, K. Yoshimura, and F. M. Grosche, arXiv:1105.3941.
[17] J. P. Remeika, G. P. Espinosa, A. S. Cooper, H. Barz, Z. Fisk, L. D. Woolf, H. C. Hamaker, M. B. Maple, G. Shirane, and W. Thomlinson, Solid State Commun. **34**, 923 (1980).
[18] S. K. Goh, D. A. Tompsett, P. J. Saines, H. C. Chang, T. Matsumoto, M. Imai, K. Yoshimura, and F. M. Grosche, Phys. Rev. Lett. **114**, 097002 (2015).
[19] P. Ehrenfest, Proc. Amsterdam Acad. **36**, 153 (1933).
[20] K. Kadowaki and S. B. Woods, Solid State Commun. **58**, 507 (1986).
[21] G. R. Stewart, Rev. Mod. Phys. **56**, 755 (1984); A. C. Hewson, *The Kondo Problem to Heavy Fermions* (Cambridge University Press, Cambridge, 1993).
[22] C. Urano, M. Nohara, S. Kondo, F. Sakai, H. Takagi, T. Shiraki, and T. Okubo, Phys. Rev. Lett. **85**, 1052 (2000).
[23] Y. Nakajima, T. Nakagawa, T. Tamegai, and H. Harima, Phys. Rev. Lett. **100**, 157001 (2008).
[24] T. Takayama, K. Kuwano, D. Hirai, Y. Katsura, A. Yamamoto, and H. Takagi, Phys. Rev. Lett. **108**, 237001 (2012).
[25] Y.-K. Kuo, C. S. Lue, F. H. Hsu, H. H. Li, and H. D. Yang, Phys. Rev. B **64**, 125124 (2001).
[26] Y. K. Kuo, K. M. Sivakumar, T. H. Su, and C. S. Lue, Phys. Rev. B **74**, 045115 (2006).
[27] C. S. Lue, H. F. Liu, S. L. Hsu, M. W. Chu, H. Y. Liao, and Y. K. Kuo, Phys. Rev. B **85**, 205120 (2012).
[28] K. Seo and S. Tewari, Phys. Rev. B **90**, 174503 (2014).
[29] T. Sakamoto, M. Wakeshima, Y. Hinatsu, and K. Matsuhira, Phys. Rev. B **75**, 060503 (2007).
[30] J. H. Kim, J.-S. Rhyee, and Y. S. Kwon, Phys. Rev. B **86**, 235101 (2012).

[31] S. C. Chen and C. S. Lue, Phys. Rev. B **81**, 075113 (2010).
[32] C. S. Lue, S. H. Yang, A. C. Abhyankar, Y. D. Hsu, H. T. Hong, and Y. K. Kuo, Phys. Rev. B **82**, 045111 (2010).
[33] C. S. Lue, S. H. Yang, T. H. Su, and B.-L. Young, Phys. Rev. B **82**, 195129 (2010).
[34] in *Metallic Shifts in NMR*, edited by G. C. Carter, L. H. Bennett, and D. J. Kahan (Pergamon, Oxford, 1977).
[35] C. S. Lue, Y. F. Tao, and T. H. Su, Phys. Rev. B **78**, 033107 (2008).
[36] C. S. Lue, T. H. Su, B. X. Xie, S. K. Chen, J. L. MacManus-Driscoll, Y. K. Kuo, and H. D. Yang, Phys. Rev. B **73**, 214505 (2006).
[37] C. S. Lue, R. F. Liu, Y. F. Fu, C. Cheng, and H. D. Yang, Phys. Rev. B **77**, 115130 (2008).
[38] C. Song, J. Park, J. Koo, K.-B. Lee, J. Y. Rhee, S. L. Bud'ko, P. C. Canfield, B. N. Harmon, and A. I. Goldman, Phys. Rev. B **68**, 035113 (2003).
[39] S. H. Curnoe, H. Harima, K. Takegahara, and K. Ueda, Phys. Rev. B **70**, 245112 (2004).
[40] M. D. Johannes and I. I. Mazin, Phys. Rev. B **77**, 165135 (2008).
[41] J. Laverock, T. D. Haynes, C. Utfeld, and S. B. Dugdale, Phys. Rev. B **80**, 125111 (2009).
[42] C. Tournier-Colletta, L. Moreschini, G. Autes, S. Moser, A. Crepaldi, H. Berger, A. L. Walter, K. S. Kim, A. Bostwick, P. Monceau, E. Rotenberg, O. V. Yazyev, and M. Grioni, Phys. Rev. Lett. **110**, 236401 (2013).
[43] F. Galli, S. Ramakrishnan, T. Taniguchi, G. J. Nieuwenhuys, J. A. Mydosh, S. Geupel, J. Ludecke, and S. van Smaalen, Phys. Rev. Lett. **85**, 158 (2000).
[44] C. H. Lee, H. Matsuhata, H. Yamaguchi, C. Sekine, K. Kihou, T. Suzuki, T. Noro, and I. Shirotani, Phys. Rev. B **70**, 153105 (2004).
[45] M. H. Lee, C. H. Chen, M.-W. Chu, C. S. Lue, and Y. K. Kuo, Phys. Rev. B **83**, 155121 (2011).
[46] M. H. Lee, C. H. Chen, C. M. Tseng, C. S. Lue, Y. K. Kuo, H. D. Yang, and M.-W. Chu, Phys. Rev. B **89**, 195142 (2014).